Interface-Mediated Crystallization Enables PEDOT:PSS-Free All-Perovskite Tandems with 29.1% Efficiency and Enhanced Durability

Fengzhu Li[1,2,9,*], Deng Wang[3,9], Jiamin Xu[1,2], Yunfan Wang[3], Wenlin Jiang[3], Jie Zeng[3,4], Mingqian Chen[3], Manuel Kober-Czerny[5], Fion Sze Yan Yeung[1,2], Sai-Wing Tsang[3], Francis R. Lin[6,7], Hin-Lap Yip[3,7], Henry J. Snaith[5], Yen-Hung Lin[1,2,5,*], Baomin Xu[4,*], Alex K.-Y. Jen[3,6,7,8,*]

[1]Department of Electronic and Computer Engineering, The Hong Kong University of Science and Technology, Clear Water Bay, Kowloon, 999077, Hong Kong SAR
[2]State Key Laboratory of Displays and Opto-Electronics, The Hong Kong University of Science and Technology, Clear Water Bay, Kowloon, 999077, Hong Kong SAR
[3]Department of Materials Science and Engineering, City University of Hong Kong, Kowloon, 999077, Hong Kong SAR
[4]Department of Materials Science and Engineering, and SUSTech Energy Institute for Carbon Neutrality, Southern University of Science and Technology, Shenzhen, 518055 China
[5]Department of Physics, University of Oxford, Clarendon Laboratory, Parks Road, Oxford OX1 3PU, UK
[6]Department of Chemistry, City University of Hong Kong, Kowloon, 999077, Hong Kong SAR
[7]Hong Kong Institute for Clean Energy, City University of Hong Kong, Kowloon, 999077, Hong Kong SAR
[8]State Key Laboratory of Marine Pollution, City University of Hong Kong, Kowloon, 999077, Hong Kong SAR
[9]These authors contributed equally: Fengzhu Li and Deng Wang.
[*]Corresponding authors. Email: eefengzhuli@ust.hk; yh.lin@ust.hk; xubm@sustech.edu.cn; alexjen@cityu.edu.hk

SUMMARY

Monolithic all-perovskite tandem solar cells (TSCs) present a promising strategy to surpass the efficiency limits of single-junction devices through bandgap engineering. However, the operational stability is hampered by hygroscopic degradation and phase segregation of PEDOT:PSS, the most common hole transport material for narrow-bandgap subcells. Here, we systematically investigate the role of interface-mediated crystallization dynamics in mixed tin-lead (Sn-Pb) perovskites through *in situ* studies. We find that the solvent-substrate synergetic interactions with PEDOT:PSS induce

metastable phase segregation within the mixed Sn-Pb perovskite during crystallization. Replacing PEDOT:PSS with a phenothiazine-functionalized interface can facilitate the direct phase transition and achieve a preferential (100) crystal orientation. This approach yields high-quality perovskite films with reduced defect density and suppressed non-radiative recombination loss, enabling single-junction mixed Sn-Pb perovskite solar cells with a power conversion efficiency (PCE) of 23.2%. Furthermore, we applied a hybrid interlayer integrating thiol and phosphonic acid anchoring groups on SnO_2/Au surface, the resulting dense interconnecting layer supports a monolithic all-perovskite TSC with a PCE of 29.1%. Additionally, the device retains 90% of the initial efficiency over 800 hours of maximum power point tracking under simulated 1-sun illumination at 40 °C, demonstrating robust operational stability.

INTRODUCTION

Metal halide perovskites have emerged as transformative materials for tandem solar cells (TSCs), driven by their exceptional absorption coefficients, low Urbach energy, tunable bandgaps, and cost-effective fabrication[1]. These characteristics position perovskite-based TSCs as prime candidates to surpass single-junction efficiency limits while enabling lightweight and flexible devices. Among various TSC configurations, all-perovskite tandems stand out by combining high efficiency, lightweight, low cost, and scalable manufacturing[2-4]. Nevertheless, mixed Sn-Pb narrow-bandgap (NBG) subcells still face two major challenges: (i) intrinsic material instability due to rapid Sn^{2+} oxidation and asynchronous Sn/Pb crystallization kinetics, which induce compositional heterogeneity and severe bulk defects[5-8]; (ii) performance and stability limitations arising from the widespread use of PEDOT:PSS as the hole-transport layer (HTL), stemming from its parasitic near-infrared absorption losses and the hygrothermal instability of PSS[9,10]. These inherent drawbacks of PEDOT:PSS hinder the development of all-perovskite TSCs, underscoring the urgent need for reliable HTL alternatives that offer broadband transparency and robust environmental stability to advance mixed Sn-Pb perovskites for tandem architectures.

Alternative HTLs such as poly[bis(4-phenyl)(2,4,6-trimethylphenyl)amine] (PTAA) and nickel oxide demonstrate improved optical transparency and thermal resilience[11-13]. However, these materials consistently underperform compared to PEDOT:PSS in single-junction mixed Sn-Pb perovskite solar cells (PSCs), attributed to their poor wettability, energy-level misalignment, and defect-rich interfaces. While self-assembled monolayers (SAMs) hold promise as hole extraction layers for efficient Pb-based PSCs, their effective implementation in mixed Sn-Pb systems remains limited[14-18]. This limitation arises from inadequate wetting of perovskite precursor solutions on SAM-modified surfaces and energy-level mismatch between mixed Pb-Sn perovskites and SAMs[15]. To address this, researchers often resort to high-temperature treatments (up to 400 °C)[19] and the mixing of different SAMs to achieve uniform coverage[14,16], yet these approaches complicate the processing and still fail to overcome the interfacial mismatch. These constraints emphasize the necessity of tailored HTL or intercontact layer (ICL) interfaces that enable optimal energy alignment and robust wetting to propel mixed Sn-Pb perovskites and their integration into all-perovskite TSCs.

In this work, we elucidate the critical role of interface-mediated crystallization dynamics in mixed Sn-Pb perovskites via multiple *in situ* characterizations. We demonstrate that the widely used PEDOT:PSS HTL engages in synergetic solvent-substrate interactions with perovskite precursors, inducing a metastable state during crystallization. *In situ* photoluminescence (PL) monitoring reveals that this metastable state triggers significant segregation of perovskite compositions, highlighting the intrinsic limitations of PEDOT:PSS. To address this, we employed a phenothiazine-functionalized phosphonic acid monolayer: 4PAPT, i.e., 4-(10H-phenothiazin-10-yl)butyl)phosphonic acid, as an alternative to engineer interfacial synergy. Time-resolved PL lifetime mapping of mixed Sn-Pb perovskite films on 4PAPT exhibits a fivefold increase in carrier lifetime relative to those on PEDOT:PSS, indicating reduced defect density and substantially suppressed non-radiative recombination losses. Benefiting from its favorable energy alignment and the predominant (100) crystal orientation on 4PAPT, single-junction mixed Sn-Pb PSCs achieved a power conversion

efficiency (PCE) of 23.2% with extended operational stability. We further translate this interfacial strategy to all-perovskite tandem devices by co-depositing phenothiazine-functionalized SAMs with thiol and phosphonic acid anchoring groups on SnO_2/Au surfaces, ensuring dense molecular assembly and robust interconnect layers. This interface-engineered architecture yields a monolithic all-perovskite TSC with a PCE of 29.1%, which is the highest efficiency reported for PEDOT:PSS-free configurations to date[16,20-22]. This approach also delivers all-SAM-based all-perovskite TSCs that demonstrate a T_{90} (*i.e.,* the time for a solar cell to degrade to 90% of its maximum efficiency) of 800 hours for continuous operation under 1-sun illumination at 40 °C, with their performance stabilizing afterwards.

RESULTS

Substrate-induced Phase Transition Asymmetry in Pb- and Sn-based Perovskites

The prevalent adoption of PEDOT:PSS in NBG perovskite originates from its high conductivity and favorable work function. However, its inherent tendency of phase separation, which gives rise to the formation of insulating PSS-rich domains, fundamentally compromises interfacial stability in NBG PSCs[23,24]. Here, we employed a phenothiazine-functionalized phosphonic acid monolayer: 4PAPT, i.e., 4-(10H-phenothiazin-10-yl)butyl)phosphonic acid, as an alternative HTL, due to its optimal highest occupied molecular orbital level alignment (-5.3 eV) with the NBG perovskites for efficient hole extraction (Figures S1-S6).

To systematically evaluate 4PAPT as an alternative to PEDOT:PSS for NBG perovskites, we performed comparative X-ray diffraction (XRD) studies of crystallization pathways on different substrates. We first tracked the crystallization pathways on 4PAPT and PEDOT:PSS substrates by comparing the phase transition between Pb-based and Sn-based perovskites, through analysis of the metastable stages and annealed films[25]. The perovskite precursor solutions were prepared by dissolving PbI_2 or SnI_2, and organic halides (formamidinium lead iodide (FAI) and methylammonium iodide (MAI)), within a mixed solvent composed of N,N-

dimethylformamide (DMF) and dimethyl sulfoxide (DMSO). As depicted in **Figure 1A**, no significant disparities were detected in films fabricated on different substrates for Pb-based perovskite. The peaks at 6.58°, 7.20°, and 9.19° correspond to the intermediate phases based on MAI[26], whereas the peak at 11.78° is attributed to the δ-phase of $FAPbI_3$. These phases were present on both substrates and subsequently transformed into the α-phase of $FAPbI_3$ following annealing. However, in the case of Sn-based perovskite, the SnI_2-3DMSO intermediate phase is observed on the PEDOT:PSS substrate[27], yet it is absent on the 4PAPT substrate, presenting a direct perovskite phase formation after spinning (**Figure 1B and C**). This observed discrepancy cannot be attributed to differences in wettability, as substantiated by the contact angle test results (Figure S7), implying that the interaction between the precursors and the substrate is of crucial importance in influencing the formation and subsequent transition of the intermediate phase.

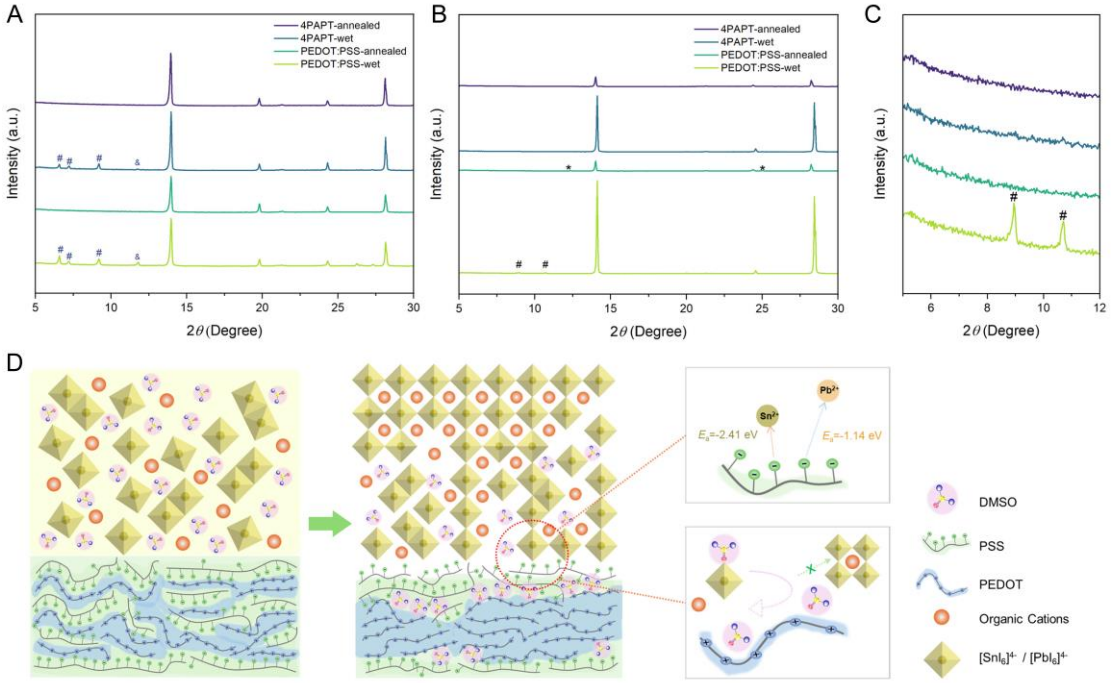

Figure 1. Substrate-induced phase transitions in lead and tin perovskites.
(A and B) XRD patterns of the as-deposited (wet) and annealed films for (A) Pb-based and (B) Sn-based perovskites on different substrates. Peaks marked with # denote the intermediate phases of precursors and solvents (panels A, B), & indicates δ-$FAPbI_3$, * designates SnI_2.
(C) Deconvoluted XRD pattern from (B), highlighting intermediate phase formation in Sn-based perovskite.
(D) Schematic illustration of the synergistic solvent-substrate interactions between

PEDOT:PSS and perovskite precursors.

It is widely recognized that the incorporation of DMSO can enhance the conductivity of PEDOT:PSS through phase separation and chain alignment, trapping DMSO within PEDOT domains while exposing PSS-rich surfaces[28] (**Figure 1D**). Critically, although SnI_2 reacts faster with FAI/MAI than PbI_2, PSS-rich surfaces exhibit stronger adsorption for Sn^{2+} (E = -2.41 eV) compared to Pb^{2+} (E = -1.14 eV) (Figure S8 and S9). Therefore, phase transition from the metastable phase to the perovskite phase is restarted in Sn-based perovskite on PEDOT:PSS, resulting in a distinct SnI_2 peak after annealing (**Figure 1B**) [29]. In parallel, trapped DMSO synergistically impedes perovskite phase transition, leading to the SnI_2-3DMSO intermediate phase on PEDOT:PSS. Conversely, the entire phase transition proceeds very rapidly on the 4PAPT substrate, facilitating direct formation from the precursor to the Sn-based perovskite (**Figure 1B**)[24,25]. Furthermore, 4PAPT accelerates DMSO desolvation through Coulombic repulsion, thereby promoting rapid perovskite nucleation with a predominant (100) crystallographic orientation. The resulting oriented crystallization not only aligns with thermodynamic stabilization pathways but also significantly suppresses defect formation, enhancing carrier mobility[30] and minimizing trap densities[31].

Metastable Phase Segregation in Mixed Sn-Pb Perovskites

To further elucidate the interface-mediated crystallization dynamics in mixed Sn-Pb perovskites, we implemented *in situ* PL monitoring during film processing (Figure S10). Perovskite films with the composition of $FA_{0.9}MA_{0.05}Cs_{0.05}Pb_{0.5}Sn_{0.5}I_3$ were deposited in an N_2-filled glovebox. Real-time phase evolution was tracked using a 450 nm laser excitation source coupled to a fiber-optic spectrometer, achieving a temporal resolution of 10 ms. Due to the inherent fiber absorption, all samples exhibited PL spectral splitting at around 940 nm[32]. As shown in **Figure 2A** and **B**, both perovskite films displayed an immediate PL intensity surge upon anti-solvent (chlorobenzene, CB) dripping, signifying the rapid perovskite nucleation and domain growth triggered by solvent extraction. Notably, the 4PAPT-based film demonstrated sustained PL enhancement, reaching a maximum intensity of four times higher than that of the

PEDOT:PSS-based film.

In contrast, the PEDOT:PSS-based film exhibited rapid PL quenching within 10 seconds after CB dripping, which can be attributed to the aggregation of perovskite emitters and the formation of high-density defects at grain boundaries[33]. Furthermore, the PL spectrum of PEDOT:PSS-based perovskite film showed peak splitting immediately after spin-coating ceased, accompanied by a blue shift and PL quenching, indicating the segregation of metastable intermediate phase into different perovskite compositions (**Figure 2C**). On the contrary, the Sn-Pb mixed perovskite film cast on the 4PAPT substrate displayed a continuous increase in PL intensity throughout the spin-coating process, with no observable peak splitting or spectral shifts (**Figure 2D**). The PL intensity only began to quench after spin-coating stopped, which is attributed to the prolonged laser illumination.

To establish a direct correlation between PL evolution and crystallization dynamics, we performed XRD analysis of metastable phases for both substrates. As shown in **Figure 2E**, the film on the PEDOT:PSS substrate exhibited a distinct peak at 7.0° and prominent SnI_2 diffraction peaks, indicating incomplete phase transition arising from synergetic solvent-substrate interactions. This chemically stabilized intermediate phase, corresponding to the peak at 7.0°, induces two critical effects: (1) interfacial phase segregation through preferential nucleation of Sn-rich domains at buried interfaces (Figure S11) [29,34], and (2) optoelectronic degradation via laser-induced decomposition of metastable phases, which is manifested as post-spin-coating PL peak splitting under continuous irradiation. Conversely, the perovskite film on the 4PAPT substrate displayed exclusive perovskite phase crystallization without any detectable intermediate or secondary phases (**Figure 2F** and Figure S12), confirming its efficacy in directing homogeneous crystallization for mixed Sn-Pb perovskites.

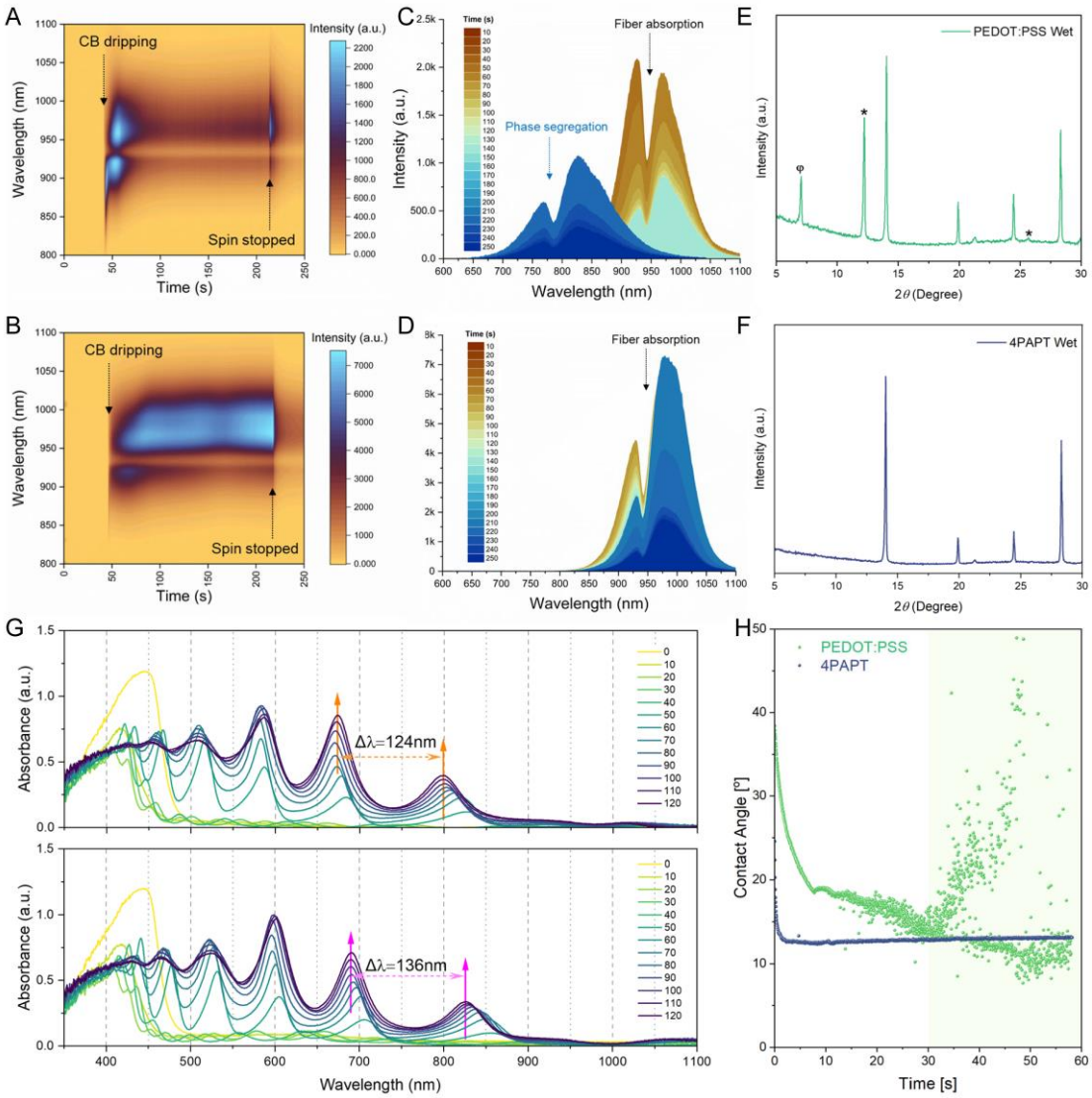

Figure 2. *In situ* characterization of crystallization dynamics in mixed Sn-Pb perovskite films.

(A and B) *In situ* PL evolution during the crystallization of mixed Sn-Pb perovskite films on (A) PEDOT:PSS and (B) 4PAPT substrates.

(C and D) Extracted PL spectra at different times during spin-coating on (C) PEDOT:PSS and (D) 4PAPT substrates.

(E and F) XRD patterns of wet perovskite films cast on (E) PEDOT:PSS and (F) 4PAPT substrates.* designates SnI_2. φ denotes an unresolved intermediate phase.

(G) *In situ* UV-vis spectra evolution during film formation on PEDOT:PSS (down) and 4PAPT (up) substrates, with time indicated in seconds.

(H) Dynamic contact angle evolution of DMSO droplets on PEDOT:PSS and 4PAPT substrates.

To gain deeper insights into the substrate-induced phase transition, we conducted the *in situ* UV-vis absorption measurements (Figure S13). We monitored the temporal evolution of wavelength and absorbance intensity over the spin-coating process. The

mixed Sn-Pb perovskite film on PEDOT:PSS exhibited a gradual increase in absorption intensity after the addition of anti-solvent (Figure S14), suggesting slower phase transition kinetics compared to those of the 4PAPT-based sample. In contrast, the 4PAPT-based film demonstrated sufficient transition of the intermediate phase to the perovskite phase upon anti-solvent dripping, evidenced by the immediate enhancement in absorbance. Furthermore, *in situ* UV-vis spectra revealed a progressive blue shift ($\Delta\lambda$ = 12 nm) in the absorption peaks for 4PAPT-based samples during spin-coating (**Figure 2G**). This blue shift is likely attributed to reduced crystallite sizes, which induce quantum confinement effects, consistent with the observations in substrate-constrained perovskite nucleation systems[35].

We also performed contact angle (CA) measurements to evaluate the substrate wettability and its implications for crystallization (Figure S15). While both substrates are hydrophilic, PEDOT:PSS provides a more hydrophilic surface with a lower CA (52.8°) compared to 4PAPT (65.8°) upon H_2O dripping. In contrast, with DMSO dripping, PEDOT:PSS exhibits a slightly higher CA (38.4°) than the 4PAPT substrate (24.6°), indicating that the surface of 4PAPT shows better wettability to perovskite precursor and has a positive effect on the moisture stability. We also tracked the evolution of CA during DMSO dripping through the time-dependent CA measurements, as shown in **Figure 2H**. The CA of PEDOT:PSS decreases from 38° to 13° over 30 s and shows substantial error distribution, thereafter, attributed to DMSO-induced substrate dissolution, as evidenced by irregular droplet spreading. In contrast, 4PAPT maintained stable CAs after wetting, indicating robust interfacial integrity during processing (Figure S16). These observations align with the interface-mediated crystallization mechanism, which positions 4PAPT as an optimal candidate for fabricating high-quality mixed Sn-Pb perovskites and their derived photovoltaics.

Suppressed Non-radiative Recombination Losses

To probe the effects of interface-mediated crystallization control on optoelectronic properties, we performed high-spatial-resolution (100 nm) confocal PL lifetime

mapping. Spatially resolved PL lifetime distributions under pulsed excitation at both top and buried interfaces are presented in **Figures 3A-3D**, providing direct access to interfacial determinants of film quality. We fit the average lifetimes with bi-exponential fitting[36]. Crucially, perovskite films on both substrates exhibited significantly extended PL lifetimes when excited through buried interfaces (τ_{buried}) versus top surfaces (τ_{top}), highlighting the dominance of trap-assisted non-radiative recombination at the untreated top surface, over charge extraction or recombination losses at the HTL/perovskite interface (**Figures 3A and 3B**). 4PAPT-based perovskite film demonstrated enhanced and near-identical lifetimes with excitation from both interfaces ($\tau_{top\text{-}S}$ = 386 ns *vs* $\tau_{buried\text{-}S}$ = 377 ns), indicative of vertically homogeneous crystallization, while PEDOT:PSS counterparts showed pronounced heterogeneity ($\tau_{top\text{-}P}$ = 73 ns vs $\tau_{buried\text{-}P}$ = 183 ns) (Figure S17). This translates to a fivefold enhancement in top-surface lifetime for 4PAPT-based films, reflecting a reduced defect density and significantly suppressed non-radiative recombination loss.

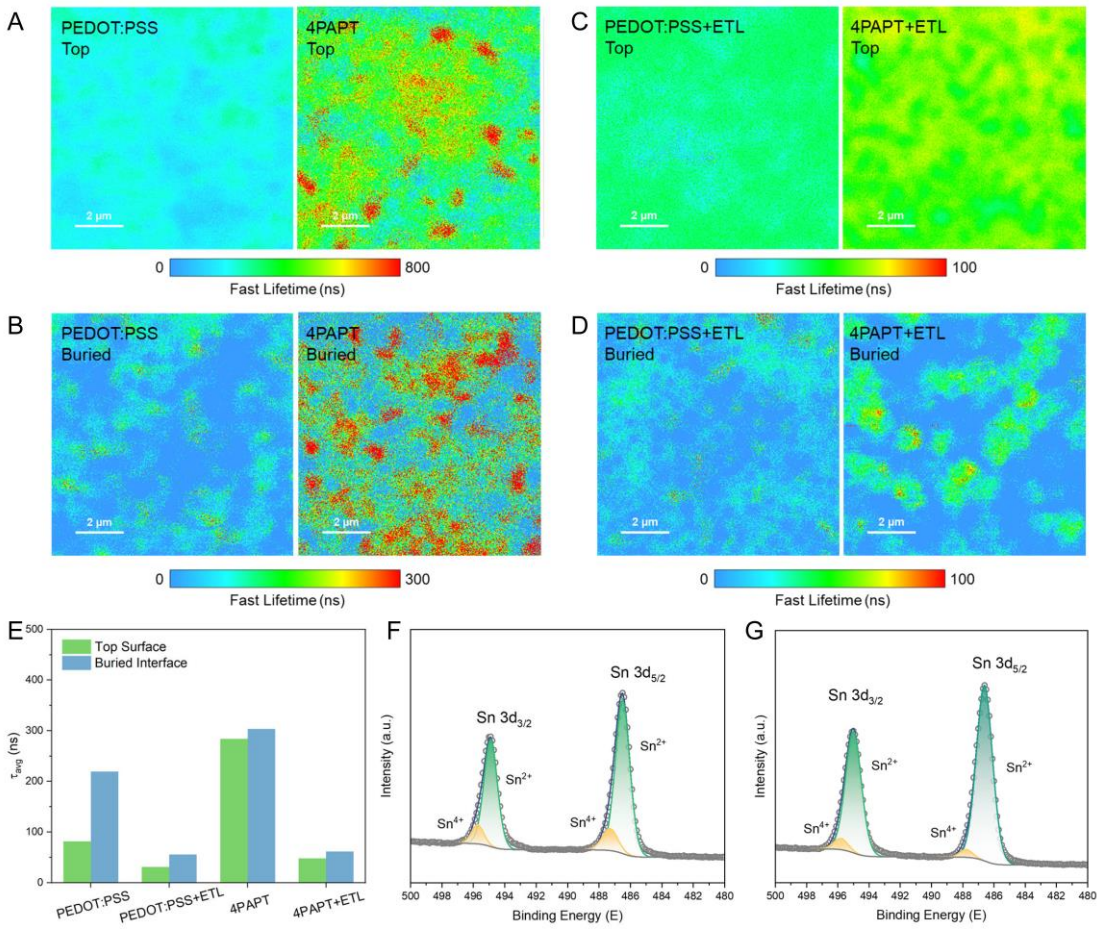

Figure 3. Defect suppression through interfacial stabilization.
(A to D) Spatially resolved PL lifetime maps under 509 nm pulsed excitation.
(E) Photoluminescence lifetime histogram of the perovskite films. Lifetimes were extracted using bi-exponential fitting.
(F and G) High-resolution Sn 3d XPS spectra for mixed Sn-Pb perovskite films on (F) PEDOT:PSS and (G) 4PAPT substrates.

We then sandwiched the perovskite films by depositing an electron transporting layer (ETL) on top to examine the charge recombination kinetics. This configuration induced a pronounced quenching of the PL decay for both systems, as depicted in **Figures 3C and 3D**. The 4PAPT-based perovskite film exhibited an extended top-surface PL lifetime ($\tau_{top\text{-}SE}$ = 47 ns) compared to the PEDOT:PSS-based film ($\tau_{top\text{-}PE}$ = 34 ns), underscoring the enhanced defect suppression of the 4PAPT substrate. The average lifetimes, derived from bi-exponential fitting analysis, further corroborated the homogeneity and enhanced quality of the 4PAPT-based perovskite films (**Figure 3E**). Additionally, we analyzed the intensity-dependent time-correlated single-photon counting (TCSPC) response of perovskite films on both substrates, fitting the TCSPC data to extract the non-radiative (k_{nr}) and radiative (k_{rad}) recombination rates (Figure S18). With k_{rad} fixed to 5×10^{-9} cm^3s^{-1} for all samples, we observed that the variation in TCSPC decay could be attributed to a substantial difference in non-radiative recombination rates, which ranged from 1.7×10^6 s^{-1} for 4PAPT substrates to 7×10^6 s^{-1} for PEDOT: PSS substrate (Figure S19 and Table S1). These findings collectively emphasize the pivotal role of interfacial engineering in optimizing perovskite film quality, not just suppressing recombination at that given interface, demonstrating that substrate choice profoundly influences defect distribution and charge recombination kinetics.

We also conducted a comprehensive analysis of the substrate's role in suppressing Sn^{4+} formation, which constitutes the primary defect in mixed Sn-Pb perovskite systems. Our X-ray photoelectron spectroscopy (XPS) analysis revealed no significant peak shifts in either Pb 4f or Sn 3d spectra, suggesting consistent perovskite compositions on different substrates (Figure S20). However, the Sn $3d_{5/2}$ and Sn $3d_{3/2}$ peaks exhibited characteristic splitting into two distinct components, corresponding to Sn^{2+} and Sn^{4+}

oxidation states. Comparative analysis demonstrated a notable difference in Sn^{4+} content between films on different substrates. The perovskite film deposited on PEDOT:PSS exhibited a substantial Sn^{4+} proportion of 13.5%, whereas 4PAPT-based films showed significantly reduced Sn^{4+} content at 5.1% (**Figures 3F** and **3G**). These findings suggest that substrate selection can influence Sn^{2+} oxidation, but it cannot completely prevent this process, necessitating the incorporation of additional antioxidants for long-term stability enhancement.

To further investigate the degradation mechanisms, we conducted aging studies and analyzed Sn^{4+} content at both surface and buried interfaces (Figure S21). The PEDOT:PSS-based films displayed substantially higher Sn^{4+} concentrations at the buried interface compared to the surface, highlighting PEDOT:PSS-induced stability challenges under ambient (Figure S22). This observation aligns with our XRD measurements of the wet perovskite films, where the PEDOT:PSS-based sample rapidly turned yellow after measurement, whereas 4PAPT-based counterpart maintained its dark feature for over 10 minutes (Figure S23), further corroborating the superior interfacial stability enabled by 4PAPT modification.

Stabilized Narrow-Bandgap Perovskite Solar Cells

To evaluate the device performance of PEDOT:PSS and 4PAPT as HTLs for mixed Sn-Pb perovskite, inverted (p-i-n structured) single-junction NBG PSCs were fabricated with a device architecture of indium tin oxide (ITO)/HTLs/NBG perovskite/C_{60}/bathocuproine (BCP)/Ag (**Figure 4A**). The best-performing PSCs based on the PEDOT:PSS exhibits a PCE of 23.03% with a V_{OC} of 0.87 V and a J_{SC} of 32.80 mA/cm^2 (Figure S24). When PEDOT:PSS is replaced with 4PAPT, a higher PCE of 23.18% is obtained, which is among the highest PCE of SAM-based mixed Sn-Pb PSCs (**Figure 4B** and Table S2). The steady-state power output (SPO) at the maximum power point of the 4PAPT-based device was boosted to 22.89%, as shown in **Figure 4C**. The integrated J_{SC} value from external quantum efficiency (EQE) measurement also agrees well with that from the *J-V* measurements (Figure S25). **Figure 4D** and Figure S26

summarize the performance of PSCs based on different HTLs, the average PCEs of PEDOT:PSS and 4PAPT-based cells are 22.20% and 22.51%, respectively. The enhanced V_{OC} can be attributed to the matched HOMO level with perovskite and the lower defect concentration in the perovskite films based on the 4PAPT substrate. The E_F of the buried perovskite shifts up by 0.18 eV (from -4.75 eV on PEDOT:PSS to -4.57 eV on the 4PAPT substrate), indicating reduced Sn^{4+} accumulation and a more n-type character in the perovskite film (Figure S27).

To gain deeper insights into the correlation between photoexcited charge carrier dynamics and device performance across different hole transport layers (HTLs), we conducted a comprehensive analysis of photovoltage and photocurrent decay behaviors in the corresponding devices. The measured data were fitted using a single exponential decay model to quantify the characteristic time constants. As illustrated in **Figure 4E**, the devices employing 4PAPT exhibited significantly prolonged charge-recombination decay time (τ_R = 0.86 μs) and shortened charge-extraction time (τ_C = 0.29 μs), in contrast to PEDOT:PSS-based devices, which showed τ_R = 0.34 μs and τ_C = 0.46 μs, respectively. The extended τ_R observed in 4PAPT-based devices correlates well with the enhanced PL lifetime of perovskite films deposited on 4PAPT substrates, while the shorter τ_C indicates more efficient charge carrier collection in these devices. These findings collectively suggest that 4PAPT can facilitate more effective hole extraction from perovskite compared to PEDOT:PSS.

To assess the long-term stability of the devices, we tracked the device performance following the international summit on organic photovoltaic stability (ISOS) protocol. As shown in **Figure 4F**, the 4PAPT-based device exhibited outstanding shelf stability, retaining 92.5% of the original PCE after 1100 hours, whereas the control PEDOT:PSS-based device only remained 81.5% of the initial PCE. The 4PAPT-based device also demonstrated superior stability compared to its PEDOT:PSS-based counterpart under ambient conditions without any encapsulation, retaining 80% of its initial efficiency after 60 minutes. In contrast, the PEDOT:PSS-based device dropped to 60 % of its initial PCE after exposure to ambient air for 60 minutes (Figure S28). Through the

exploration of ions distribution of perovskite films after aging, we found that the PSS^- could migrate to the bulk of the perovskite film, leading to the fatal degradation of perovskite (**Figures 4G and 4H**). This observation agrees well with our previous results of the substrate-induced metaphase separation and the easy degradation of the PEDOT:PSS-based mixed Sn-Pb perovskite films.

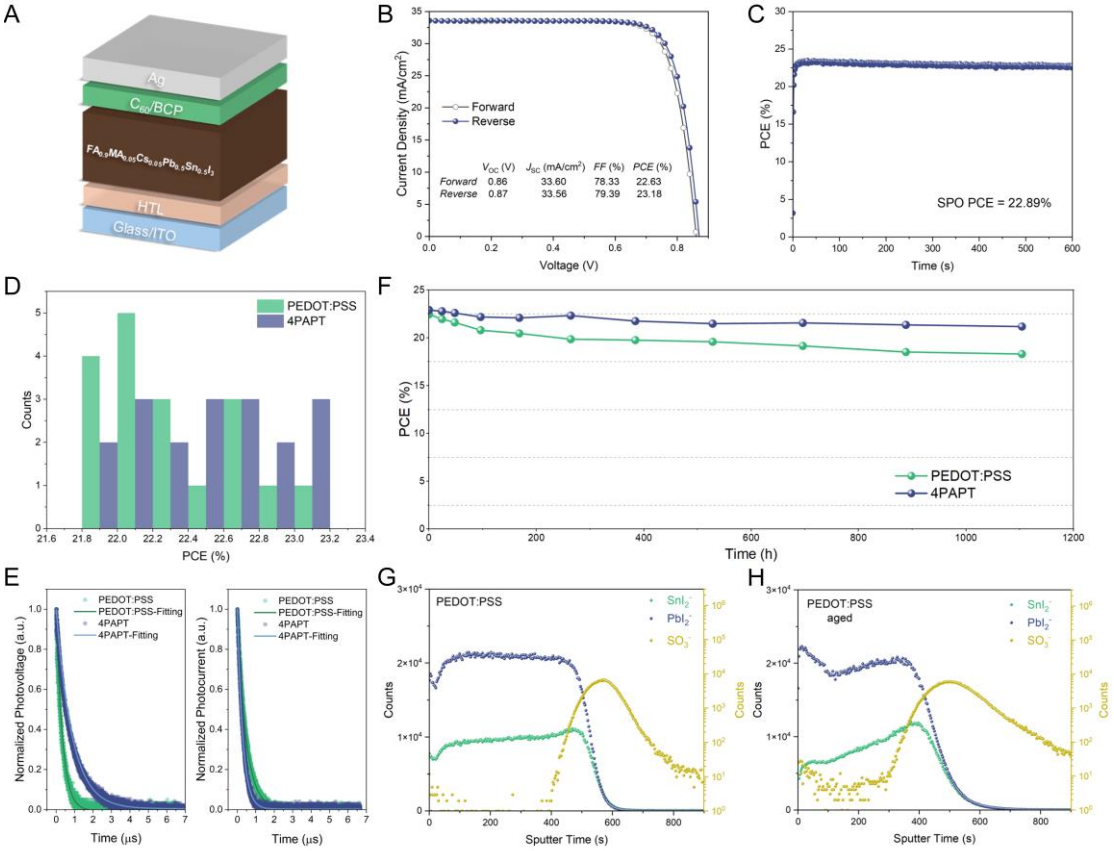

Figure 4. Photovoltaic performance of single-junction NBG PSCs.
(A) Device structure of the single-junction PSC based on different HTLs.
(B) *J-V* curves of the champion PSCs based on 4PAPT.
(C) Steady-state power output (SPO) of the champion devices based on 4PAPT.
(D) PCE distributions of different HTL-based PSCs (18 devices).
(E) The transient photovoltage and transient photocurrent measurements of the single-junction PSCs based on different HTLs.
(F) Shelf stability test of PSCs with different HTLs based on the ISOS-D1 protocol. The devices were aged in an N_2-filled glovebox without any encapsulation.
(G and H) TOF-SIMS depth profile of elements in perovskite films based on PEDOT:PSS substrate (G) before and (H) after aging.

All-Perovskite Tandems via Hybrid Interface Engineering

We then fabricated two-terminal (2T) all-perovskite TSCs with 4PAPT for NBG

perovskite and a top cell with the composition of $FA_{0.8}Cs_{0.2}Pb(I_{0.6}Br_{0.4})_3$. Detailed information about the wide-bandgap (WBG) top cells can be found in Supplementary Information. The tandem devices have a structure of glass/ITO/CbzNaph/WBG perovskite/C_{60}/SnO_2/Au/HTL/NBG perovskite/C_{60}/BCP/Ag, where CbzNaph is (4-(7H-dibenzo[c,g]carbazol-7-yl)butyl)phosphonic acid[37] (**Figure 5A**). The HTL for NBG perovskite is based on PEDOT:PSS and 4PAPT. Given that the evaporated thin Au layer (1 nm) exhibits an island distribution and the SnO_2 surface is exposed[38,39], we utilized a hybrid SAMs strategy with thiol (4-(10H-phenothiazin-10-yl)butane-1-thiol, 4SHPT) and phosphate (4PAPT) anchoring groups to achieve a dense assembly (Figures S29 and S30). The champion device based on the hybrid strategy showed a PCE of 29.09 %, with a V_{OC} of 2.13 V, a J_{SC} of 16.35 mA/cm^2, and a *FF* of 83.54 %, surpassing the PEDOT:PSS-based device (PCE of 28.45%) (Figure S31). The device demonstrated a SPO efficiency of 28.7 % at the maximum power point (Figure S32), which is the highest PCE of PEDOT:PSS-free all-perovskite TSCs reported so far (**Figure 5C**). The integrated J_{SC} values of the WBG and NBG sub-cells obtained from the EQE spectra are 16.68 and 16.24 mA/cm^2, respectively, in good agreement with the J_{SC} values determined from *J-V* measurements (Figure S33). This enhanced current density is attributed to the increased transmittance of the SAM substitution (Figure S34). We also fabricated ICL-only devices and analyzed their current density-voltage curves (Figure S35). The ICL with the PEDOT:PSS displayed a diode-like *J-V* characteristic under a positive bias voltage, indicating the presence of a Schottky-type contact barrier for the charge carrier injection into the ICL[40]. In contrast, the hybrid SAM-based ICLs displayed nearly linear *J-V* curves, suggesting the formation of a quasi-Ohmic contact at the ICLs.

To further assess the operational stability of tandem cells, we recorded the encapsulated devices using maximum power point (MPP) tracking under simulated 1-sun illumination at approximately 40 °C (**Figure 5D**). The tandem cell with hybrid strategy maintained over 90% of its initial efficiency after 800 hours of continuous operation under AM1.5G illumination, with a linear extrapolation to a T_{90} over 1100 hours (T_{90}

means the time for a solar cell to degrade to 90% of its maximum efficiency). While the control tandem cells with PEDOT:PSS demonstrated a fast decay and dropped to 80% of their initial performance after 400 hours [41]. This significantly enhanced device stability can be primarily attributed to the replacement of lethal PEDOT:PSS and the improved interfacial contact with perovskite, characterized by the reduced non-radiative recombination loss and the facilitated charge transport.

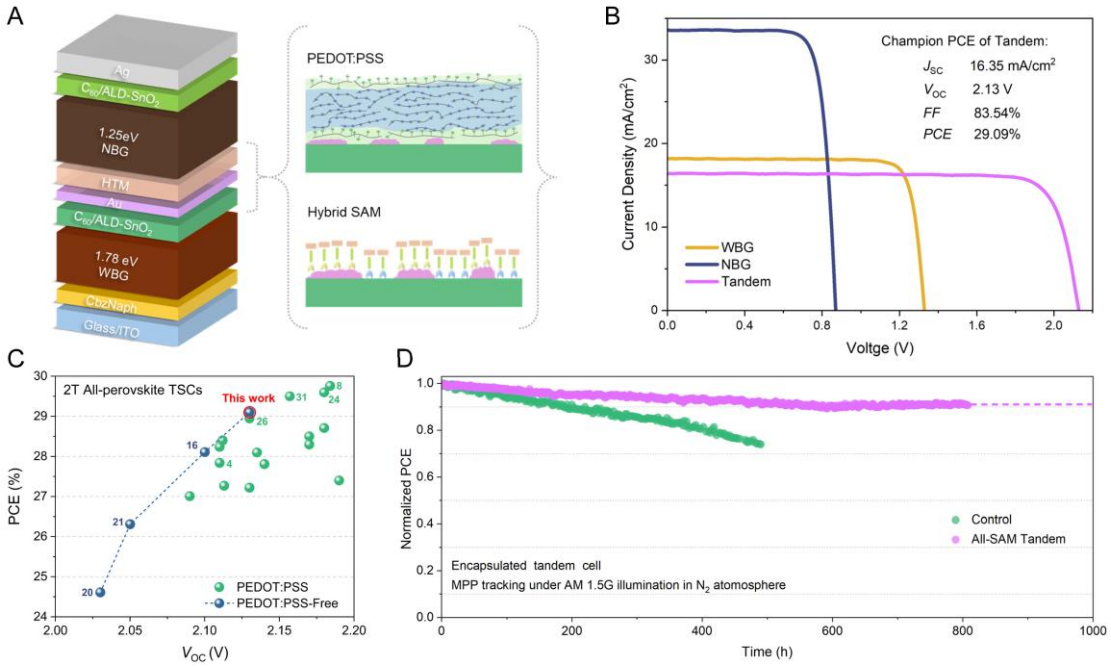

Figure 5. Device performance of 2T all-perovskite TSCs.

(A) Schematic illustration of the 2T all-perovskite TSCs architecture employing PEDOT:PSS and hybrid SAMs as HTL.

(B) J-V characteristics of champion NBG, WBG, and all-perovskite tandem devices based on a hybrid strategy.

(C) Statistical distribution of PCE and Voc for recently reported all-perovskite TSCs using PEDOT:PSS versus PEDOT:PSS-free HTLs. The numbers next to the symbol refer to the specific reference, and all corresponding references are summarized in Table S3.

(D) MPP tracking of the all-perovskite TSCs under simulated one-sun illumination, with dashed lines indicating lifetime evolution modeled by linear extrapolation. No extra heating or cooling was applied to the devices during the MPP tracking. The temperature of the devices under continuous illumination is around 40 °C, as measured by infrared thermometers.

DISCUSSION

In summary, we elucidate the critical role of interface-mediated crystallization dynamics in achieving high-performance NBG photovoltaics. By employing 4PAPT as

the hole-selective contact, we have demonstrated a high-quality mixed Sn-Pb perovskite film characterized by direct phase transition, preferred crystal orientation, and reduced nonradiative recombination loss. These synergistic effects yield single-junction NBG solar cells with a PCE of 23.2%, while the implementation of a hybrid interlayer integrating thiol and phosphonic acid anchoring groups on SnO_2/Au ensures dense molecular assembly and robust interconnecting. This further boosts the efficiency of monolithic all-perovskite tandems to a record PCE of 29.1% – the highest reported for PEDOT:PSS-free configurations so far. Remarkably, the tandem device based on the hybrid SAMs maintains 90% of its initial performance under continuous 1-sun illumination for over 800 hours, establishing exceptional operational stability benchmarks for all-perovskite TSCs. Although some key findings have been revealed, the atomic-scale configuration of PEDOT:PSS-induced metastable phases requires multidisciplinary resolution. Future investigations combining experimental studies and computational molecular simulations will be essential to advance universally adaptable interface engineering strategies across diverse photovoltaic device architectures.

METHODS

Materials

All the solvents are purchased from J&K and are used as received, including N, N-dimethylformamide (99.8%, super dry, with molecular sieves), dimethyl sulfoxide (99.9%, super dry), isopropanol (99.5%, super dry), and chlorobenzene (99.90%, J&K). Caesium iodide (CsI), cesium bromide (CsBr), methylammonium iodide (MAI), formamidinium iodide (FAI), and formamidinium bromide (FABr) were bought from Dysol. PbI_2 (99.9985%) and lead bromide ($PbBr_2$) were bought from TCI. Methylammonium chloride (MACl), ethylenediamine dihydroiodide ($EDAI_2$), PEDOT:PSS (AI4083), bathocuproine (BCP, 99.9%), and C_{60} were bought from Xi'an Polymer Light Technology. 4-guanidinobenzoic acid hydrochloride (GBAC, 99%), tin powder (99.5%), Tin fluoride (SnF_2), tin iodide (SnI_2, 99.99%), and aluminum oxide nanoparticles (20 wt.% % in isopropanol) were bought from Sigma-Aldrich.

Piperazinium iodide (PI) [42] and CbzNaph [37] were synthesized according to previous reports. 4PAPT is bought from Luminescence Technology Corp. (Lumtec). 2-amino-3-mercaptopropanoic acid hydrochloride (AMPH) is purchased from Macklin Biochemical Technology Co., Ltd.

Materials Synthesis

The reagents and starting materials were commercially available and used without any further purification, if otherwise specified. 10*H*-phenothiazine is purchased from TCI.

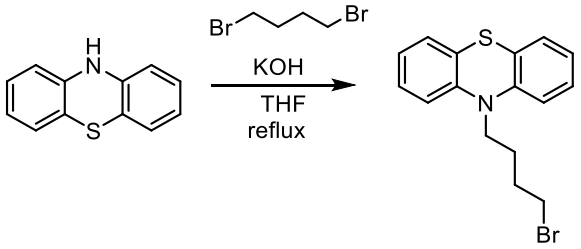

10-(4-bromobutyl)-10*H*-phenothiazine: To a stirred suspension of 10*H*-phenothiazine (2 g, 0.01 mol) in 30 mL of THF was added sodium hydroxide (2.81 g, 0.05 mol). The obtained solution was stirred for 30 min at 45 °C, and 1,4-dibromobutane (6.48 g, 0.03 mol) was added. After refluxing for 8 h, the reaction mixture was evaporated under reduced pressure, and the residue was washed with water, filtered, and dried. The product was purified by silica gel column chromatography using a mixture of petroleum ether and DCM (2:1 *v*:*v*) as eluent to obtain 10-(4-bromobutyl)-10*H*-phenothiazine as a white solid (1.78 g, yield=53%). ^{1}H NMR (300 MHz, Chloroform-*d*) δ 7.17 (m, 1.6 Hz, 4H), 6.99 – 6.84 (m, 4H), 3.99 – 3.84 (m, 2H), 3.40 (td, *J* = 5.1, 4.1, 2.5 Hz, 2H), 2.03 – 1.90 (m, 4H) (Figure S1). ^{13}C NMR (75 MHz, Chloroform-*d*) δ 145.1, 127.6, 127.3, 125.5, 122.7, 115.6, 46.2, 33.5, 29.9, 25.3 (Figure S2).

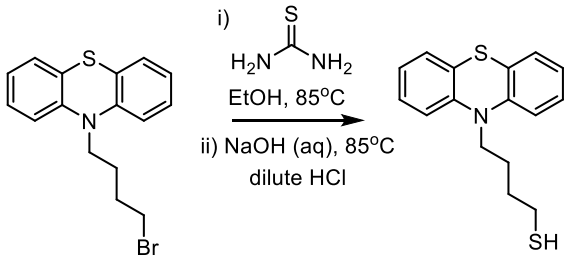

4-(10*H*-phenothiazin-10-yl)butane-1-thiol: A mixture of the 10-(4-bromobutyl)-10*H*-phenothiazine precursor (1 g, 3 mmol), thiourea (1.14 g, 5 eq, 14.9 mmol), and anhydrous ethanol (18 mL) was heated at 85℃. After 6 h, the solvent was evaporated under vacuum pressure, and 20% aqueous sodium hydroxide solution (10 mL) was added. After another 4 hours of reaction at 85°C, the reaction is completed. After cooling, the reaction mixture was acidified by diluting hydrochloric acid to pH=4~5, and then was extracted with dichloromethane. The organic phase was dried over Na_2SO_4, then decompression evaporation and mixed with silica gel powder, and purified by silica gel chromatography column (n-hexane: dichloromethane, v/v=5/1) to obtain 4-(10*H*-phenothiazin-10-yl)butane-1-thiol as a white solid (0.53 g, yield=62%). ^{1}H NMR (300 MHz, Chloroform-*d*) δ 7.20 – 7.11 (m, 4H), 6.96 – 6.83 (m, 4H), 3.88 (t, *J* = 6.8 Hz, 2H), 2.54 (q, *J* = 7.3 Hz, 2H), 1.92 (dtd, *J* = 8.8, 7.5, 6.1 Hz, 2H), 1.80 – 1.69 (m, 2H), 1.31 (t, *J* = 7.8 Hz, 1H) (Figure S3). ^{13}C NMR (75 MHz, Chloroform-*d*) δ 145.1, 127.6, 127.2, 125.3, 122.6, 115.6, 46.7, 31.3, 25.5, 24.3 (Figure S4).

Perovskite precursor preparation

The NBG mixed Sn-Pb perovskite precursor solution (1.8 M) was prepared by dissolving FAI, MAI, CsI, PbI_2, and SnI_2, in DMF:DMSO mixed solvent (3:1= v:v) with the chemical formula of $FA_{0.7}MA_{0.25}Cs_{0.05}Pb_{0.5}Sn_{0.5}I_3$. 5 mol% of SnF_2, 2 mol% of tin powder, and 1 mol% of AMPH [32] were added into the precursor. Then, the precursor solution was stirred at room temperature for at least 3 hours and filtered through a 0.22 μm PTFE filter before use.

The WBG perovskite precursor solution (1.2 M) was prepared by dissolving FAI, CsI, PbI_2, $PbBr_2$ in DMF: DMSO mixed solvent (4:1= v:v) with the chemical formula of $FA_{0.8}Cs_{0.2}Pb(I_{0.6}Br_{0.4})_3$. Additionally, 0.5 mol% of GBAC [33] was added to the perovskite precursor and stirred at room temperature for 2 hours.

Device fabrication

Fabrication of single-junction NBG PSCs

The prepatterned indium tin oxide (ITO) glass substrates were sequentially washed by

sonication with detergent (Decon 90), deionized water, and isopropanol for 15 min. The washed ITO glass was dried in an 85 °C oven for over 12 h. Then, the cleaned substrates were subjected to ultraviolet ozone (UVO) for 30 min. After that, PEDOT:PSS filtered through a 0.22 μm PES filter was spin-coated on ITO substrates at 5000 rpm for 30 s and annealed on a hotplate at 140°C for 25 min in ambient air. After cooling, the substrates were transferred to the N_2-filled glovebox. For the SAM-based HTL, the UV/ozone-treated substrates were immediately transformed into an N_2-filled glovebox. 30 μL of the SAM solution (1 mg/mL in IPA) was spin-coated on fresh substrates at 3000 rpm for 30 s, followed by annealing at 100 °C for 15 min. After cooling down, the diluted aluminum oxide nanoparticle dispersion (1:150 vol% in IPA) was dynamically spin-coated on the substrates at 5000 rpm for 30 s and annealed at 100 °C for 5 min [43]. Then, 50 μL of the prepared NBG precursor solution was spin-coated at 1000 rpm for 10 s and 5000 rpm for 40 s; 180 μL of CB as antisolvent was dripped onto the film at 18 s before the end of the procedure. The substrates were then annealed at 100°C for 10 min. After deposition of the perovskite active layer, 50 μL of $EDAI_2$ solution (0.3 mg/mL in IPA) was dynamically coated onto perovskite films at 5000 rpm for 30 s and followed by annealing at 100°C for 5 min. Finally, C_{60} (25 nm), BCP (8 nm), and Ag(100 nm) were sequentially deposited on top of the perovskite by thermal evaporation under a high vacuum (<4 × 10−6 torr).

Fabrication of all-perovskite tandem solar cells

We fabricated all-perovskite tandem solar cells with a device configuration of ITO/CbzNaph/WBG perovskite/C_{60}/ALD-SnO_2/Au/PEDOT:PSS or SAM/NBG perovskite/C_{60}/BCP/Cu. The cleaned ITO glass substrates were UV/ozone treated and transferred to the N_2-filled glovebox for SAM deposition. CbzNaph solution (1 mg/mL in IPA) was spin-coated on ITO substrates at 3000 rpm for 30 s and annealed on a hotplate at 100°C for 15 min. After cooling down, the substrates were washed by pure IPA through spin coating at 3000 rpm for 30 s and annealed at 100°C for 5 min. Then, 50 μL of the WBG precursor solution was spin-coated at 1000 rpm for 10 s and 4000 rpm for 40 s; 200 μL of CB as antisolvent was dripped onto the film at 20 s before

the end of the procedure. The substrates were then transferred onto a hotplate and heated at 100°C for 10 min. After cooling down, PI solution (0.3 mg/mL in IPA) was dynamically coated onto perovskite films at 5000 rpm for 30 s and annealed at 100°C for 5 min. After cooling, the substrates were transferred to an evaporation system for the deposition of C_{60} film (25 nm) onto the WBG perovskites. Then, the films were transferred into the ALD chamber for depositing a SnO_2 (20 nm) layer, followed by depositing a 1 nm-Au layer through thermal evaporation. Next, diluted PEDOT:PSS with IPA (1:1, v/v) was coated onto the bottom substrates at 5000 rpm for 40 s and annealed at 100°C for 5 min. The substrates were then transferred to an N_2-filled glovebox for the fabrication of NBG films. For SAM-based HTL, 30 μL of the mixed SAM solution (4PAPT-4SHPT = 1:1; 1 mg/mL in IPA) was spin-coated on the substrates at 3000 rpm for 30 s, followed by annealing at 100 °C for 10 min. After cooling down, pure IPA was dynamically spin-coated on the substrates and then annealed at 100 °C for 5 min. The NBG films were deposited and treated as described above. Finally, C_{60} (25 nm), BCP (8 nm), and Ag(100 nm) were sequentially deposited onto NBG perovskite to complete the tandem device fabrication. Additionally, a 100 nm MgF_2 layer was thermally deposited onto the back of ITO glass as an anti-reflection layer.

Material and device characterization

The ^{1}H NMR spectra were recorded on a Bruker AVANCE III HD 300 MHz spectrometer in a DMSO-d6 solution with tetramethylsilane as a reference. The morphology of the samples was recorded by an SEM instrument (Philips XL30 FEG). The XPS and UPS characterization measurements were conducted in a VG ESCALAB 220i XL surface analysis system equipped with a He-discharge lamp ($h\nu$ = 21.22 eV) and a monochromatic Al Kα X-ray gun ($h\nu$ = 1,486.60 eV), respectively. ToF-SIMS (ION TOF-SIMS5) data were analyzed with the positive mode (Bi) under 30 keV (1.00 pA) with an area of 100 × 100 μm^2. The sputter parameters for the device are O_2 under 1 keV (100 nA) with an area of 300 × 300 μm^2, and the sputter parameters for the film sample are a gas cluster ion beam ion gun under 10 keV (10 nA) with an area

of 800 × 800 μm^2. XRD characterization was conducted on a D2 Phaser instrument with Cu Kα (wavelength, 1.5418 Å) radiation. The *in-situ* PL and UV-Vis absorption techniques were set inside a temperature-controlled nitrogen-filled glovebox, and the laser intensity was maintained at 8 mW/cm^2. A specialized spin-coating holder and hotplate were utilized to eliminate background noise in the PL signals. Time-resolved PL mapping and lifetime were measured by a PicoQuant Micro Time 100 confocal microscope system. An Olympus 50× objective (LCPLFLN) with a numerical aperture of 0.7 was used for the measurement. The samples were packaged and measured in a dark environment to minimize the influence of ambient light. The sample was excited using a 510 nm picosecond pulse laser with a full width of approximately 6.2 nm, and 8the collected signal was passed through a 532 nm long-pass filter. The repetition frequency selected for the test was 200 kHz. The contact angle was measured using a high-precision optical tensiometer (Biolin Theta) following the sessile drop method. The *J-V* characteristics were measured in an N_2-filled glovebox by a Keithley 2400 source meter and an Enlitech Solar Simulator SS-F7-3A, which offered the simulated AM 1.5G illumination (100 mW/cm^2). The light intensity was calibrated using a silicon solar cell (with a KG-2 filter) from the National Renewable Energy Laboratory. The *J-V* curves of devices were obtained from a forward scan and reverse scan with a scanning rate of 0.01 V/s and a delay time of 10 ms. The solar cell's active area (0.04 cm^2) was defined by the aperture of the metal mask. The stabilized power output (SPO) was obtained by applying the maximum output bias. The EQE was measured by a DSR100UV-B spectrometer with an SR830 lock-in amplifier. The operational stability was evaluated using an MPP tracking system (91PVKSolar Co., Ltd, China). The unencapsulated devices were tested under AM 1.5G illumination (100 mW/cm^2) in an N_2-filled chamber. The illumination was generated using an LED-lamp-based solar simulator. There is no extra heating or cooling to the devices during the MPP tracking. The temperature of the devices under continuous illumination is around 40 °C, as measured by infrared thermometers. The transient photocurrent (TPC) and transient photovoltage decays (TPV) were obtained by a transient photoelectric streamer voltage

measurement system (South-Port SP-TPVC). Considering DMSO as a polar solvent, all structures were optimized and characterized in DMSO with the SMD solvent model (SCRF=SMD) at B3LYP-D3/BSI level, BSI representing a basis set with SDD for Pd, Sn, I, and 6-31G(d) for other atoms. Harmonic frequency analysis calculations at the same level were performed to verify that the optimized geometries are minima (no imaginary frequency). The energies were further improved by B3LYP/BSII//B3LYP-D3/BSI single-point calculations with solvent effects accounted by the SMD solvent model, using the experimental solvent (DMSO). BSII denotes a basis set with SDD for Pd, Sn, I, and 6-311++G(d,p) for other atoms. All DFT calculations were carried out using the Gaussian 09 program. Selected computed structures are illustrated using the CYLview. A TimeHarp300 (Picoquant) was used to measure the TCSPC response of perovskite halfstacks. The 800 nm thick samples were photo-excited by a 635 nm pulsed laser with a repetition rate of 1 MHz. Each sample was illuminated from the substrate- and material-side at fluences of 2.8×10^{9} cm^{-2} and 2.8×10^{10} cm^{-2}. The pile-up rate was kept below 5% to ensure only single photons were counted.

RESOURCE AVAILABILITY

Lead contact

Further information and requests for resources and materials should be directed to and will be fulfilled by the lead contact, Prof. Alex Jen (alexjen@cityu.edu.hk).

Materials availability

This study did not generate new, unique materials.

Data and code availability

This study did not generate any datasets. All data needed to evaluate the conclusions in the paper are present in the paper or the supplemental information. All the data are available from the corresponding authors upon reasonable request.

ACKNOWLEDGMENTS

A.K.Y.J. thanks the sponsorship of the Lee Shau-Kee Chair Professor (Materials

Science), and the support from the APRC Grants (9380086, 9610419, 9610440, 9610492, 9610508) of the City University of Hong Kong, the MHKJFS Grant (MHP/054/23), TCFS grant (GHP/121/22SZ) and MRP Grant (MRP/040/21X) from the Innovation and Technology Commission of Hong Kong, the Green Tech Fund (202020164) from the Environment and Ecology Bureau of Hong Kong, and the GRF grants (11304424, 11307621, 11316422) and CRS grants (CRS_CityU104/23, CRS_HKUST203/23) from the Research Grants Council of Hong Kong. This work was also financially supported by the National Key Research and Development Project from the Ministry of Science and Technology of China (Grant No. 2021YFB3800101), the Guangdong Basic and Applied Basic Research Foundation (Grant Nos. 2023B1515120031 and 2022A1515110413), the Shenzhen Science and Technology Innovation Committee (Grants Nos. JCYJ20220818100211025, SGDX20230116091649013, and KCXST20221021111616039), SUSTech Energy Institute for Carbon Neutrality (High level of special funds, G03034K001), and the Project for Building a Science and Technology Innovation Center Facing South Asia and Southeast Asia (202403AP140015). Y.-H.L. also acknowledges support from the Early Career Scheme (no. 26210623) from the Hong Kong Research Grant Council. This work was funded by UK Research and Innovation (UKRI) under the UK government's Horizon Europe funding Guarantee [grant number 10055025]. The VALHALLA project has received funding from the European Union's Horizon Europe research and innovation program under grant agreement No. 101082176. Views and opinions expressed are however those of the author(s) only and do not necessarily reflect those of the European Union or RIA. Neither the European Union nor the granting authority can be held responsible for them. F. L., J. X., F. S. Y. Y. and Y.-H. L. acknowledge support from the State Key Laboratory of Displays and Opto-Electronics. F. L. is grateful to Dr. Shuaifeng Hu and Dr. Junke Wang for their kind support during her visit. The authors would like to acknowledge Prof. Alex Jen for his outstanding contributions to the field. This work is respectfully dedicated in honor of his 70th birthday.

AUTHOR CONTRIBUTIONS

F. L., Y.-H. L. and A. J. conceived the idea and directed the project. F. L. and D. W. fabricated the major devices and conducted the characterizations, and M. C. assisted in the preparation of WBG subcells. J. X. conducted the contact angle and TOF-SIMS tests. F. L. and Y. W. collected the *in situ* PL and UV-vis data with the supervision of S.-W. T., W. J. developed the synthesis of 4SHPT. J. Z. conducted the TPV and TPC tests. M. K. -C. conducted the TCSPC and analyzed the results with the supervision of H. J. S.. F. L. wrote the manuscript and revised it with D. W., F. R. L., H.-L. Y., Y.-H. L., B. X., and A. J. All authors discussed the results and commented on the paper.

DECLARATION OF INTERESTS

The authors declare that they have no competing interests. H.J.S. is a cofounder and chief scientific officer of Oxford PV Ltd.

SUPPLEMENTAL INFORMATION

Supplemental information can be found online at xxxxxx.

REFERENCES

1. Kojima, A., Teshima, K., Shirai, Y., and Miyasaka, T. (2009). Organometal Halide Perovskites as Visible-Light Sensitizers for Photovoltaic Cells. Journal of the American Chemical Society *131*, 6050-6051. 10.1021/ja809598r.
2. Xiao, K., Lin, Y.-H., Zhang, M., Oliver, R.D.J., Wang, X., Liu, Z., Luo, X., Li, J., Lai, D., Luo, H., et al. (2022). Scalable processing for realizing 21.7%-efficient all-perovskite tandem solar modules. Science *376*, 762-767. 10.1126/science.abn7696.
3. Tong, J., Jiang, Q., Ferguson, A.J., Palmstrom, A.F., Wang, X., Hao, J., Dunfield, S.P., Louks, A.E., Harvey, S.P., Li, C., et al. (2022). Carrier control in Sn–Pb perovskites via 2D cation engineering for all-perovskite tandem solar cells with improved efficiency and stability. Nat. Energy *7*, 642-651. 10.1038/s41560-022-01046-1.
4. Zhou, S., Fu, S., Wang, C., Meng, W., Zhou, J., Zou, Y., Lin, Q., Huang, L., Zhang, W., Zeng, G., et al. (2023). Aspartate all-in-one doping strategy enables efficient all-perovskite tandems. Nature *624*, 69-73. 10.1038/s41586-023-06707-z.
5. Lin, R., Xiao, K., Qin, Z., Han, Q., Zhang, C., Wei, M., Saidaminov, M.I., Gao, Y., Xu, J., Xiao, M., et al. (2019). Monolithic all-perovskite tandem solar cells with 24.8% efficiency exploiting comproportionation to suppress Sn(ii) oxidation in precursor ink. Nature Energy *4*, 864-873. 10.1038/s41560-019-0466-3.
6. Gao, H., Xiao, K., Lin, R., Zhao, S., Wang, W., Dayneko, S., Duan, C., Ji, C., Sun, H.,

Bui, A.D., et al. (2024). Homogeneous crystallization and buried interface passivation for perovskite tandem solar modules. Science *383*, 855-859. 10.1126/science.adj6088.

7. Hu, S., Thiesbrummel, J., Pascual, J., Stolterfoht, M., Wakamiya, A., and Snaith, H.J. (2024). Narrow Bandgap Metal Halide Perovskites for All-Perovskite Tandem Photovoltaics. Chem. Rev. *124*, 4079-4123. 10.1021/acs.chemrev.3c00667.
8. Hu, S., Wang, J., Zhao, P., Pascual, J., Wang, J., Rombach, F., Dasgupta, A., Liu, W., Truong, M.A., Zhu, H., et al. (2025). Steering perovskite precursor solutions for multijunction photovoltaics. Nature *639*, 93-101. 10.1038/s41586-024-08546-y.
9. Prasanna, R., Leijtens, T., Dunfield, S.P., Raiford, J.A., Wolf, E.J., Swifter, S.A., Werner, J., Eperon, G.E., de Paula, C., Palmstrom, A.F., et al. (2019). Design of low bandgap tin–lead halide perovskite solar cells to achieve thermal, atmospheric and operational stability. Nat. Energy *4*, 939-947. 10.1038/s41560-019-0471-6.
10. Cameron, J., and Skabara, P.J. (2020). The damaging effects of the acidity in PEDOT:PSS on semiconductor device performance and solutions based on non-acidic alternatives. Mater. Horiz. *7*, 1759-1772. 10.1039/C9MH01978B.
11. Sun, Y., Lai, Y., and Yang, Y. (2024). Progress of Hole-Transport Layers in Mixed Sn-Pb Perovskite Solar Cells. Small *20*, 2406991. https://doi.org/10.1002/smll.202406991.
12. Lee, S., Ryu, J., Lee, D.-G., Pandey, P., Oh, C.-M., Hwang, I.-W., Cho, S., Yoon, S., Lee, J.-Y., and Kang, D.-W. (2024). Unprecedented inorganic HTL-based MA-free Sn–Pb perovskite photovoltaics with an efficiency over 23%. Energy Environ. Sci. *17*, 8140-8150. 10.1039/D4EE03579H.
13. Zhou, Y., Wang, Z., Jin, J., Zhang, X., Zou, J., Yao, F., Zhu, Z., Cui, X., Zhang, D., Yu, Y., et al. (2023). Manipulation of the Buried Interface for Robust Formamidinium-based Sn−Pb Perovskite Solar Cells with NiOx Hole-Transport Layers. Angew. Chem. Int. Ed. *62*, e202300759. https://doi.org/10.1002/anie.202300759.
14. Kapil, G., Bessho, T., Sanehira, Y., Sahamir, S.R., Chen, M., Baranwal, A.K., Liu, D., Sono, Y., Hirotani, D., Nomura, D., et al. (2022). Tin–Lead Perovskite Solar Cells Fabricated on Hole Selective Monolayers. ACS Energy Letters *7*, 966-974. 10.1021/acsenergylett.1c02718.
15. Pitaro, M., Alonso, J.S., Di Mario, L., Garcia Romero, D., Tran, K., Zaharia, T., Johansson, M.B., Johansson, E.M.J., and Loi, M.A. (2023). A carbazole-based self-assembled monolayer as the hole transport layer for efficient and stable Cs0.25FA0.75Sn0.5Pb0.5I3 solar cells. J. Mater. Chem. A *11*, 11755-11766. 10.1039/D3TA01276J.
16. Liu, C., Lin, R., Wang, Y., Gao, H., Wu, P., Luo, H., Zheng, X., Tang, B., Huang, Z., Sun, H., et al. (2023). Efficient All-Perovskite Tandem Solar Cells with Low-Optical-Loss Carbazolyl Interconnecting Layers. Angew. Chem. Int. Ed. *62*, e202313374. https://doi.org/10.1002/anie.202313374.
17. Zhang, Z., Zhu, R., Tang, Y., Su, Z., Hu, S., Zhang, X., Zhang, J., Zhao, J., Xue, Y., Gao, X., et al. (2024). Anchoring Charge Selective Self-Assembled Monolayers for Tin–Lead Perovskite Solar Cells. Adv. Mater. *36*, 2312264. https://doi.org/10.1002/adma.202312264.
18. Bati, A.S.R., Liu, C., Gilley, I.W., Musgrave, C.B., Maxwell, A., Steele, J.A., Yang, Y., Chen, H., Wan, H., Xu, J., et al. (2025). A chemically bonded monolayer interface

enables enhanced thermal stability and efficiency in Pb-Sn perovskite solar cells. Joule, 102047. https://doi.org/10.1016/j.joule.2025.102047.

19. Song, D., Narra, S., Li, M.-Y., Lin, J.-S., and Diau, E.W.-G. (2021). Interfacial Engineering with a Hole-Selective Self-Assembled Monolayer for Tin Perovskite Solar Cells via a Two-Step Fabrication. ACS Energy Lett. *6*, 4179-4186. 10.1021/acsenergylett.1c02124.
20. Yu, Z., Yang, Z., Ni, Z., Shao, Y., Chen, B., Lin, Y., Wei, H., Yu, Z.J., Holman, Z., and Huang, J. (2020). Simplified interconnection structure based on C60/SnO2-x for all-perovskite tandem solar cells. Nature Energy *5*, 657-665. 10.1038/s41560-020-0657-y.
21. Yu, Z., Wang, J., Chen, B., Uddin, M.A., Ni, Z., Yang, G., and Huang, J. (2022). Solution-Processed Ternary Tin (II) Alloy as Hole-Transport Layer of Sn–Pb Perovskite Solar Cells for Enhanced Efficiency and Stability. Adv. Mater. *34*, 2205769. https://doi.org/10.1002/adma.202205769.
22. Gao, H., Lu, Q., Xiao, K., Han, Q., Lin, R., Liu, Z., Li, H., Li, L., Luo, X., Gao, Y., et al. (2021). Thermally Stable All-Perovskite Tandem Solar Cells Fully Using Metal Oxide Charge Transport Layers and Tunnel Junction. Solar RRL *5*, 2100814. https://doi.org/10.1002/solr.202100814.
23. Rivnay, J., Inal, S., Collins, B.A., Sessolo, M., Stavrinidou, E., Strakosas, X., Tassone, C., Delongchamp, D.M., and Malliaras, G.G. (2016). Structural control of mixed ionic and electronic transport in conducting polymers. Nat. Commun. *7*, 11287. 10.1038/ncomms11287.
24. Wang, J., Hu, S., Zhu, H., Liu, S., Zhang, Z., Chen, R., Wang, J., Shi, C., Zhang, J., Liu, W., et al. (2025). Mercapto-functionalized scaffold improves perovskite buried interfaces for tandem photovoltaics. Nat. Commun. *16*, 4917. 10.1038/s41467-025-59891-z.
25. Yang, X., Ma, T., Hu, H., Ye, W., Li, X., Li, M., Zhang, A., Ge, C., Sun, X., Zhu, Y., et al. (2025). Understanding and manipulating the crystallization of Sn–Pb perovskites for efficient all-perovskite tandem solar cells. Nat. Photonics *19*, 426-433. 10.1038/s41566-025-01616-1.
26. Chen, S., Xiao, X., Chen, B., Kelly, L.L., Zhao, J., Lin, Y., Toney, M.F., and Huang, J. Crystallization in one-step solution deposition of perovskite films: Upward or downward? Sci. Adv. *7*, eabb2412. 10.1126/sciadv.abb2412.
27. Jiang, X., Li, H., Zhou, Q., Wei, Q., Wei, M., Jiang, L., Wang, Z., Peng, Z., Wang, F., Zang, Z., et al. (2021). One-Step Synthesis of SnI2·(DMSO)x Adducts for High-Performance Tin Perovskite Solar Cells. J. Am. Chem. Soc. *143*, 10970-10976. 10.1021/jacs.1c03032.
28. Lu, B., Yuk, H., Lin, S., Jian, N., Qu, K., Xu, J., and Zhao, X. (2019). Pure PEDOT:PSS hydrogels. Nat. Commun. *10*, 1043. 10.1038/s41467-019-09003-5.
29. Yang, J., Wang, Z., Zhao, X., Gao, W., Xing, G., Wang, X., Wang, L., Li, C., Wang, Y., Ren, Y., et al. (2025). Guiding vertical growth and improving the buried interface of Pb–Sn perovskite films with 2D perovskite seeds for efficient narrow-bandgap perovskite solar cells and tandems. Energy Environ. Sci. *18*, 2883-2894. 10.1039/D4EE05948D.
30. Liu, Z., Lin, R., Wei, M., Yin, M., Wu, P., Li, M., Li, L., Wang, Y., Chen, G., Carnevali,

V., et al. (2025). All-perovskite tandem solar cells achieving >29% efficiency with improved (100) orientation in wide-bandgap perovskites. Nat. Mater. *24*, 252-259. 10.1038/s41563-024-02073-x.

31. Ma, C., Eickemeyer, F.T., Lee, S.-H., Kang, D.-H., Kwon, S.J., Grätzel, M., and Park, N.-G. (2023). Unveiling facet-dependent degradation and facet engineering for stable perovskite solar cells. Science *379*, 173-178. 10.1126/science.adf3349.
32. Wang, D., Chen, M., Lei, X., Wang, Y., Bao, Y., Huang, X., Zhu, P., Zeng, J., Wang, X., Tsang, S., et al. (2024). All-In-One Additive Enabled Efficient and Stable Narrow-Bandgap Perovskites for Monolithic All-Perovskite Tandem Solar Cells. Adv. Mater. *36*, 2411677. https://doi.org/10.1002/adma.202411677.
33. Li, F., Deng, X., Shi, Z., Wu, S., Zeng, Z., Wang, D., Li, Y., Qi, F., Zhang, Z., Yang, Z., et al. (2023). Hydrogen-bond-bridged intermediate for perovskite solar cells with enhanced efficiency and stability. Nat. Photonics *17*, 478-484. 10.1038/s41566-023-01180-6.
34. Zhou, J., Qiu, H., Wen, T., He, Z., Zou, C., Shi, Y., Zhu, L., Chen, C.-C., Liu, G., Yang, S., et al. (2023). Acidity Control of Interface for Improving Stability of All-Perovskite Tandem Solar Cells. Adv. Energy Mater. *13*, 2300968. https://doi.org/10.1002/aenm.202300968.
35. Demchyshyn, S., Roemer, J.M., Groiß, H., Heilbrunner, H., Ulbricht, C., Apaydin, D., Böhm, A., Rütt, U., Bertram, F., Hesser, G., et al. Confining metal-halide perovskites in nanoporous thin films. Sci. Adv. *3*, e1700738. 10.1126/sciadv.1700738.
36. Péan, E.V., Dimitrov, S., De Castro, C.S., and Davies, M.L. (2020). Interpreting time-resolved photoluminescence of perovskite materials. Phys. Chem. Chem. Phys. *22*, 28345-28358. 10.1039/D0CP04950F.
37. Jiang, W., Li, F., Li, M., Qi, F., Lin, F.R., and Jen, A.K.Y. (2022). π-Expanded Carbazoles as Hole-Selective Self-Assembled Monolayers for High-Performance Perovskite Solar Cells. Angew. Chem. Int. Ed. *61*, e202213560. https://doi.org/10.1002/anie.202213560.
38. Gaspar, D., Pimentel, A.C., Mateus, T., Leitão, J.P., Soares, J., Falcão, B.P., Araújo, A., Vicente, A., Filonovich, S.A., Águas, H., et al. (2013). Influence of the layer thickness in plasmonic gold nanoparticles produced by thermal evaporation. Sci. Rep. *3*, 1469. 10.1038/srep01469.
39. Zheng, J., Wang, G., Duan, L., Duan, W., Jiang, Y., Pearce, P., Gao, Y., Mahmud, M.A., Liao, C., Leung, T.L., et al. (2025). Tailoring nanoscale interfaces for perovskite–perovskite–silicon triple-junction solar cells. Nat. Nanotechnol. 10.1038/s41565-025-02015-x.
40. Yang, H., Chen, W., Yu, Y., Shen, Y., Yang, H., Li, X., Zhang, B., Chen, H., Cheng, Q., Zhang, Z., et al. (2023). Regulating Charge Carrier Recombination in the Interconnecting Layer to Boost the Efficiency and Stability of Monolithic Perovskite/Organic Tandem Solar Cells. Adv. Mater. *35*, 2208604. https://doi.org/10.1002/adma.202208604.
41. Chen, B., Yu, Z., Onno, A., Yu, Z., Chen, S., Wang, J., Holman, Z.C., and Huang, J. Bifacial all-perovskite tandem solar cells. Sci. Adv. *8*, eadd0377. 10.1126/sciadv.add0377.

42. Li, F., Deng, X., Qi, F., Li, Z., Liu, D., Shen, D., Qin, M., Wu, S., Lin, F., Jang, S.-H., et al. (2020). Regulating Surface Termination for Efficient Inverted Perovskite Solar Cells with Greater Than 23% Efficiency. Journal of the American Chemical Society *142*, 20134-20142. 10.1021/jacs.0c09845.
43. Lin, Y.-H., null, V., Yang, F., Cao, X.-L., Dasgupta, A., Oliver, R.D.J., Ulatowski, A.M., McCarthy, M.M., Shen, X., Yuan, Q., et al. (2024). Bandgap-universal passivation enables stable perovskite solar cells with low photovoltage loss. Science *384*, 767-775. 10.1126/science.ado2302.